Optical Determination of Gate -Tunable Bandgap in Bilayer Graphene

Yuanbo Zhang*[1], Tsung-Ta Tang*[1], Caglar Girit[1], Zhao Hao[2,4], Michael C. Martin[2], Alex Zettl[1,3], Michael F. Crommie[1,3], Y. Ron Shen[1,3] and Feng Wang[†1]

[1] Department of Physics, University of California at Berkeley, Berkeley, CA 94720, USA

[2] Advanced Light Source Division, Lawrence Berkeley National Laboratory, Berkeley, CA 94720, USA

[3] Materials Science Division, Lawrence Berkeley National Laboratory, Berkeley, CA 94720, USA

[4] Earth Sciences Division, Lawrence Berkeley National Laboratory, Berkeley, CA 94720, USA

[†] To whom correspondence should be addressed. Email: fengwang76@berkeley.edu

One sentence summary:

An unusual gate-tunable bandgap in graphene bilayers with magnitude as high as 200 meV has been demonstrated through bandedge infrared absorption, opening the door to new field-tunable electronic and photonic applications.

Abstract:

Electronic bandgaps are a defining property of solid state materials. Metals, for example, are characterized by the absence of a bandgap, while semiconductors and insulators possess non-zero gaps between conduction and valence bands. In two-dimensional graphene bilayers this bandgap can be varied continuously from zero to finite values through electrical gating. Using infrared micro-spectroscopy combined with electronic transport measurements, we demonstrate unambiguously this unusual gate-tuanble bandgap through bandedge absorption in dual-gate graphene bilayer devices. Gate-induced bandgaps up to 200 meV are achieved, strongly suggestive of applications in molecular-scale electronic and photonic devices.

Two dimensional (2D) graphene has emerged as an exciting new material displaying novel physical phenomena (*1-8*) as well as great technological potential (*9-13*). Graphene's 2D hexagonal lattice leads to a unique electronic structure (*1, 2*) that can be modified via nanopatterning (*10, 12, 13*), interlayer coupling (*14*), and the application of electrical/magnetic fields (*1, 2, 8, 15*). Of particular importance is the potential for controlling the graphene bandgap, which plays a defining role in semiconductor transport and optical properties.

Monolayer and bilayer graphene are intrinsically gapless, but the possibility of inducing controlled bandgaps in these materials has been actively pursued. For monolayer graphene this has been achieved through quantum confinement in nanoribbons (*10, 12, 13, 16*). For bilayer graphene bandgaps can be induced by applying an electric field across the bilayer (*14, 17*). Such an induced bandgap has been observed in chemically doped epitaxial graphene (*18, 19*). To explore new physics and device applications, a *continuously tunable bandgap through electrical gating* is highly desirable. Such control has proven elusive. Electrical transport measurements on gated bilayer exhibit insulating behavior only at temperatures below 1K, suggesting a bandgap value much lower than theoretical predictions (*20*). Optical studies of bilayers have been limited to samples with only a bottom electrical gate (*8, 21-23*), causing the observed spectral responses to be dominated by carrier doping effects and obscuring any signatures of a gate-induced bandgap. Such lack of experimental evidence has cast doubts on the possibility of achieving gate-controlled bandgaps in graphene bilayers (*23*).

In this report we unambiguously demonstrate the existence of a gate-tunable bandgap in bilayer graphene through the use of optical absorption spectroscopy measurements. By

equipping a bilayer sample with both top and bottom gates we are able to independently control the graphene. This allows us to separate the bandgap opening and carrier doping effects. Gate-induced bandgaps in our devices were probed using infrared absorption spectroscopy in a microscopy setup. Such optical determination of electronic bandgaps is desirable because it is generally less affected by defects or doping than electrical transport measurements. Using this technique, we were able to observe direct transitions across the gate-induced bandgap that could be continuously tuned up to 200 meV. This novel capability also enabled us to discover an unexpected Fano resonance between graphene interband electronic transitions and an optical phonon excitation. Because the bilayer tunable bandgap can be much larger than the room-temperature thermal energy, bilayer graphene holds great promise for an array of novel electronic and photonic devices.

An optical microscope image of a typical dual-gate graphene bilayer device is displayed in Fig. 1A. Graphene bilayer flakes were exfoliated from graphite and deposited onto Si/SiO_2 wafers as described in Ref. (*24*). Bilayers were identified by optical contrast in a microscope and subsequently confirmed via Raman spectroscopy(*25*). Source and drain electrodes (Au, thickness 30nm) for transport measurement (to be discussed later) were deposited directly onto the graphene bilayer through a stencil mask in vacuum. The doped Si substrate under a 285 nm thick SiO_2 layer was used as the bottom gate. The top gate was formed by sequential deposition of an 80-nm thick Al_2O_3 film and a sputtered strip of 20-nm Pt film. The Pt electrode was electrically conductive and optically semi-transparent. The cross-section view of a bilayer device is sketched in Fig. 1B. Infrared transmission spectra of the dual-gated bilayer were

obtained using the synchrotron-based IR source from the Advanced Light Source at Berkeley and a micro- Fourier transform infrared spectrometer.

The electronic structure near the Fermi level of a pristine AB stacking graphene bilayer features two nearly parallel conduction bands above two nearly parallel valence bands (Fig. 1D) (*26*). In the absence of gating, the lowest conduction band and highest valence band touch each other with a zero bandgap. Upon electrical gating, the top and bottom electrical displacement fields D_t and D_b (Fig. 1C) produce two effects (Fig. 1D): The difference of the two, $\Delta D = D_b - D_t$, leads to a net carrier doping, i.e., a shift of the Fermi energy (E_F), and the average of the two, $\bar{D} = (D_b + D_t)/2$, breaks the inversion symmetry of the bilayer and generates a non-zero bandgap (Δ) (*14, 17, 19*). By setting ΔD to zero and varying $\bar{D}$, we can tune the bandgap while keeping the bilayer charge neutral. Sets of D_b and D_t with values that yield $\Delta D = 0$ define the bilayer "charge neutral points" (CNPs). By varying ΔD above or below zero, we can inject electrons or holes into the bilayer and shift the Fermi level. In our experiment the drain electrode is grounded and the displacement fields D_t and D_b are tuned independently by top (V_t) and bottom gate voltages (V_b) through the relation $D_{b(t)} = +(-)\varepsilon_{b(t)} (V_{b(t)} - V^0_{b(t)}) / d_{b(t)}$. Here $\varepsilon_{b(t)}$ and $d_{b(t)}$ are the dielectric constant and thickness of the bottom (top) dielectric layer and $V^0_{b(t)}$ is the effective bottom (top) offset voltage due to initial environment induced carrier doping.

The relationship between $D_{b(t)}$ and $V_{b(t)}$ can be determined experimentally through electrical transport measurement (*20*). Figure 1E shows the measured resistance along the graphene plane as a function of V_t with V_b fixed at different values, and CNPs can be

identified by the peaks in the resistance curves since charge neutrality results in a maximum resistance. The deduced CNPs, in terms of (V_t, V_b), are plotted in Fig. 1F. V_t and V_b are linearly related with a slope given by $-(\epsilon_b d_t)/(\epsilon_t d_b) \approx 0.14$, consistent with an ϵ_b (thermal SiO_2) of 3.9 and ϵ_t (amorphous Al_2O_3) of 8. The peak resistance differs at different CNPs (Fig. 1E) because the field-induced bandgap itself differs. Lower peak resistance comes from a smaller bandgap and the lowest peak resistance thus identifies the zero-bandgap CNP ($D_b = D_t = 0$), allowing us to determine the offset top and bottom gate voltages from environment doping to be $V_t^0 \approx$ -7 V and $V_b^0 \approx 20$ V.

To directly probe the tunable bilayer bandgap we employed infrared micro-spectroscopy (*8, 21*). Fig. 2B shows the gate-induced bilayer absorption spectra at CNPs ($\Delta D = 0$) with $\bar{D}$=1.0 V/nm, 1.4 V/nm, and 1.9 V/nm. The absorption spectrum of the sample at the zero-bandgap CNP ($\bar{D}$=0) has been subtracted as a background reference in order to eliminate contributions to the absorption from the substrate and gate materials. Two distinct features are present in the spectra, a gate-dependent peak below 250 meV and a dip centered around 400 meV. These arise from different optical transitions between bilayer electronic bands, as illustrated in Fig. 2A. Transition I is the tunable bandgap transition that accounts for the gate-induced spectral response at energies lower than 250 meV. Transitions II, III, IV, and V occur at and above the energy of parallel band separation, γ@400 meV, and contribute to the spectral feature near 400 meV.

The absorption peak below 250 meV in Fig. 2B has pronounced gate tunability: it gets stronger and shifts to higher energy with increasing $\bar{D}$. This arises from the fact that as the bandgap increases, so does the density of states at the band edge. The position of the absorption peak, corresponding to the bandgap, increases from 150 meV at

$\bar{D}$=1.4V/nm to 200 meV at $\bar{D}$=1.9 V/nm. This shows directly that the bandgap can be continuously tuned up to at least 200 meV by electrical gating. We also note that the absorption peak in Fig. 2B is accompanied by a very sharp spectral feature at 1585 cm^{-1}(~ 200 meV). This narrow resonance can be attributed to the well known zone-center G-mode phonon in graphene (*25*). The asymmetric lineshape originates from Fano interference between the phonon and electronic (bandgap) transitions.

When the displacement field $\bar{D}$ is small (< 1.2 V/nm) , the gate-induced bandgap becomes too small and weak to be measured directly., However, it can still be extracted from the gate-induced spectral features around 400 meV. This is achieved by measuring the difference in bilayer absorption for ΔD=0 (CNP) and ΔD=0.15V/nm (electron doped) at different fixed $\bar{D}$. Such absorption difference spectra are displayed in Fig. 3A. To understand the bilayer absorption difference due to electron doping, we examine the optical transitions in Fig. 2A. With electrons occupying the conduction band states, transition IV gets stronger from extra filled initial states and transition III gets weaker less available empty final states. However, the transition IV feature is more prominent because all such transitions have similar energy due to the nearly parallel conduction bands and it gives rise to the observed peaks in the absorption difference spectra. When the bandgap increases with increasing $\bar{D}$, the lower conduction band moves up, but the upper conduction band hardly changes, making the separation between the two bands smaller. This will lead to a redshift of transitions IV. Therefore, the shift of the peak in the difference spectrum can yield the bilayer bandgap when compared to theory. When the gate-induced bandgap is small, this shift equals roughly half of the bandgap energy.

At higher $\bar{D}$, deviation from the near-parallel band picture becomes significant and the red shift saturates.

Quantitative determination of the gate-induced bandgap is obtained through comparison of our data to theoretical predictions. We model the bilayer absorption using the tight-binding model following Ref. (*22*), except that the bandgap was`here treated as a fitting parameter. Fig. 2C shows the resulting calculated gated-induced absorption spectra and extracted bandgaps of bilayer graphene in the "large bandgap" regime (**D**>120 meV). Agreement with the experimental spectra (Fig. 2B) is excellent, except for the phonon contribution which is not included in our model. For the "small bandgap" regime (**D**<120 meV), we are able to determine the bilayer bandgap by comparing our model calculations to the measured absorption difference spectra shown in Fig. 3A. Our calculations (Fig. 3B) provide a good qualitative fit to the absorption peak that arises from electron transition IV: this absorption peak shifts to lower energy as the bandgap becomes larger, reproducing the observed behavior at increasing displacement field $\bar{D}$ in Fig. 3A. Such comparison allows us to quantitatively extract the bilayer bandgap at different $\bar{D}$ in the "small bandgap" regime.

Fig. 4 shows a plot of the experimentally derived gate-tunable bilayer bandgap over the entire range (0<**D**<200 meV) as a function of applied displacement field $\bar{D}$ (symbols). Our experimental bandgap results are compared to predictions based on self-consistent tight-binding calculations (blue curve) and *ab inito* density functional calculations (red curve)(*17*). The density functional calculation using the local density approximation appears to overestimate screening effects in graphene, especially in the

weak gating regime. The phenomenological tight-binding model, on the other hand, describes our experimental results quite well.

In conclusion, we have unambiguously measured the direct bandgap induced by electrical gating in graphene bilayers, which can be continuously tuned over 200 meV. This gate-controlled bandgap offers exciting possibilities for investigation of the fundamental behavior of massive Dirac electrons and the graphene pseudo-spin degree of freedom(*27*). Combined with graphene's remarkable electrical, thermal, and mechanical properties, the extra control offered by a tunable bilayer bandgap should lead to significant advanced in nanoelectronics and in tunable, multispectral optoelectronic nanodevices.

Fig.1: Dual-gated bilayer graphene. (A) Optical microscopy image of the bilayer device. (B) Illustration of a cross-section view of the gated device. (C) Sketch showing how gating of bilayer induces top (D_t) and bottom electrical displacement fields(D_b). (D) Electronic structure of a pristine bilayer having zero bandgap. Upon gating, the displacement fields induces a non-zero bandgap (**D**) and a shift of electron Fermi energy (E_F). (E) Graphene electrical resistance as a function of top gate voltage (V_t) at different fixed bottom gate voltages (V_b). The resistance peak in each curve corresponds to the CNP (ΔD=0) for a given bottom gate voltage. (F) The linear relation between top and bottom gate voltages that results in bilayer CNPs.

Fig. 2: (A) Allowed optical transitions between different subbands in a graphene bilayer. (B) Gate-induced absorption spectra at CNP for different applied displacement fields $\bar{D}$ (with spectrum for zero-bandgap CNP subtracted as reference). Dashed black lines are a guie to the eye highlighting the low energy absorption peaks due to gate-tunable bandgap transitions I. The sharp asymmetric resonance observed near 200 meV is due to Fano resonance of the zone center G-mode phonon with continuum electronic transitions. The broad feature around 400 meV is due to electronic transitions II, III, IV and V. (C) Theoretical prediction of the gate-induced absorption spectra based on a tight-binding model where the bandgap value is taken as an adjustable parameter. The fit provides an accurate determination of the gate-tunable bandgap at strong electrical gating.

Fig. 3: (A) Absorption difference between electron doped (ΔD = 0.15 V/nm) and charge neutral bilayer (ΔD = 0) at different average displacement fields $\bar{D}$. The absorption peak is mainly due to increased absorption between nearly parallel conduction bands from extra filled initial states. The absorption peak shifts to lower energy due to the opening of the bilayer bandgap at increasing $\bar{D}$. (B) Calculated absorption difference spectra based on a tight binding model using the gate-induced bandgap as an adjustable parameter. Good qualitative agreement with the experimental data yields the gate-induced bilayer bandgap at weak gating.

Fig. 4: Gate-tunable bandgap energy of graphene bilayer as a function of gate-induced electric displacement field $\bar{D}$. This is compared to theoretical predictions based on self-consistent tight-binding (blue trace) and *ab inito* density functional calculations (red trace).

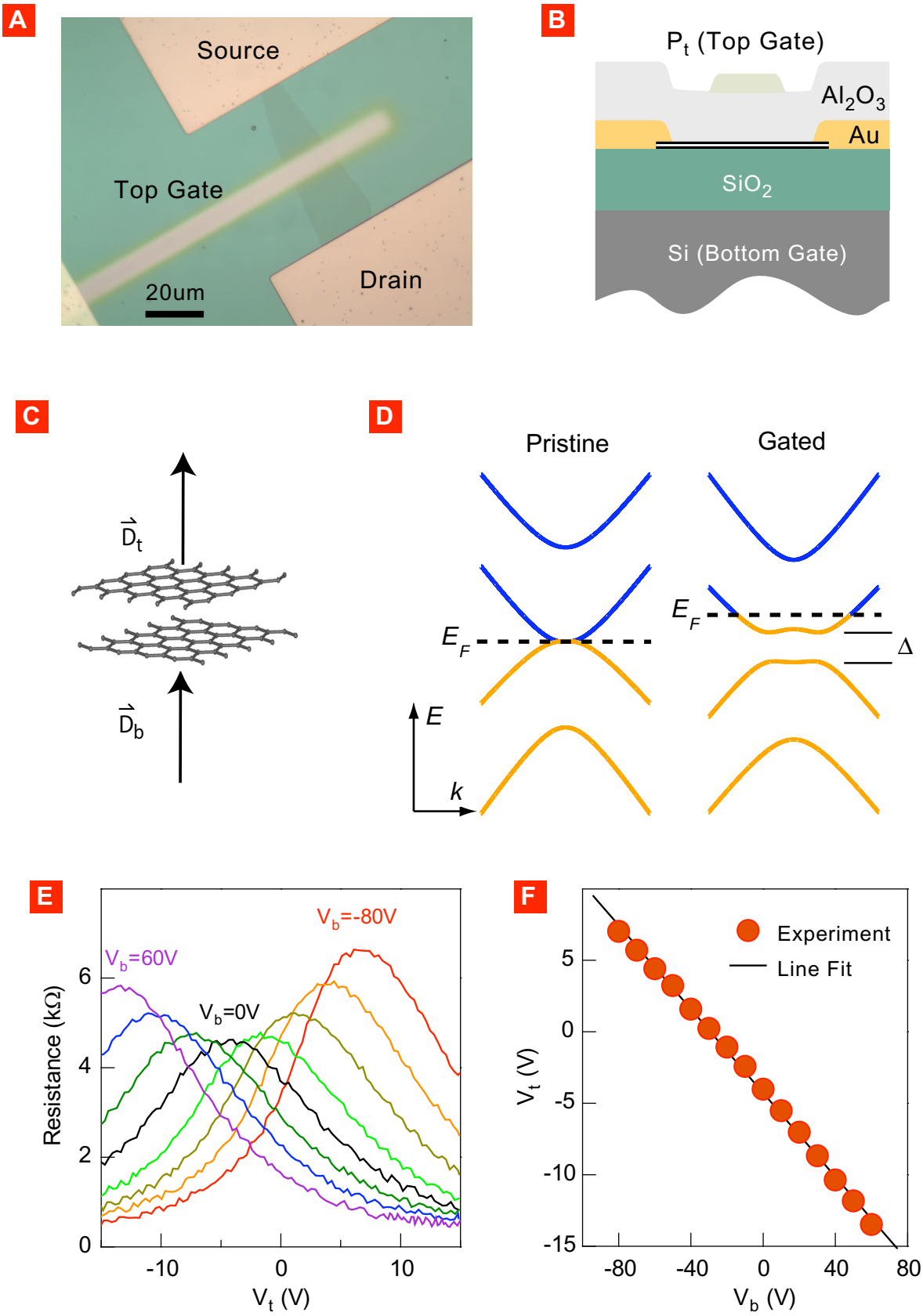
A
Source
Top Gate
Drain
20um
B
P_t (Top Gate)
Al_2O_3
Au
SiO_2
Si (Bottom Gate)
C
$\vec{D}_t$
$\vec{D}_b$
D
Pristine
Gated
E_F
E_F
Δ
E
k
E
F
V_b=-80V
V_b=60V
V_b=0V
Resistance (kΩ)
V_t (V)
Experiment
Line Fit
V_t (V)
V_b (V)

Figure 1

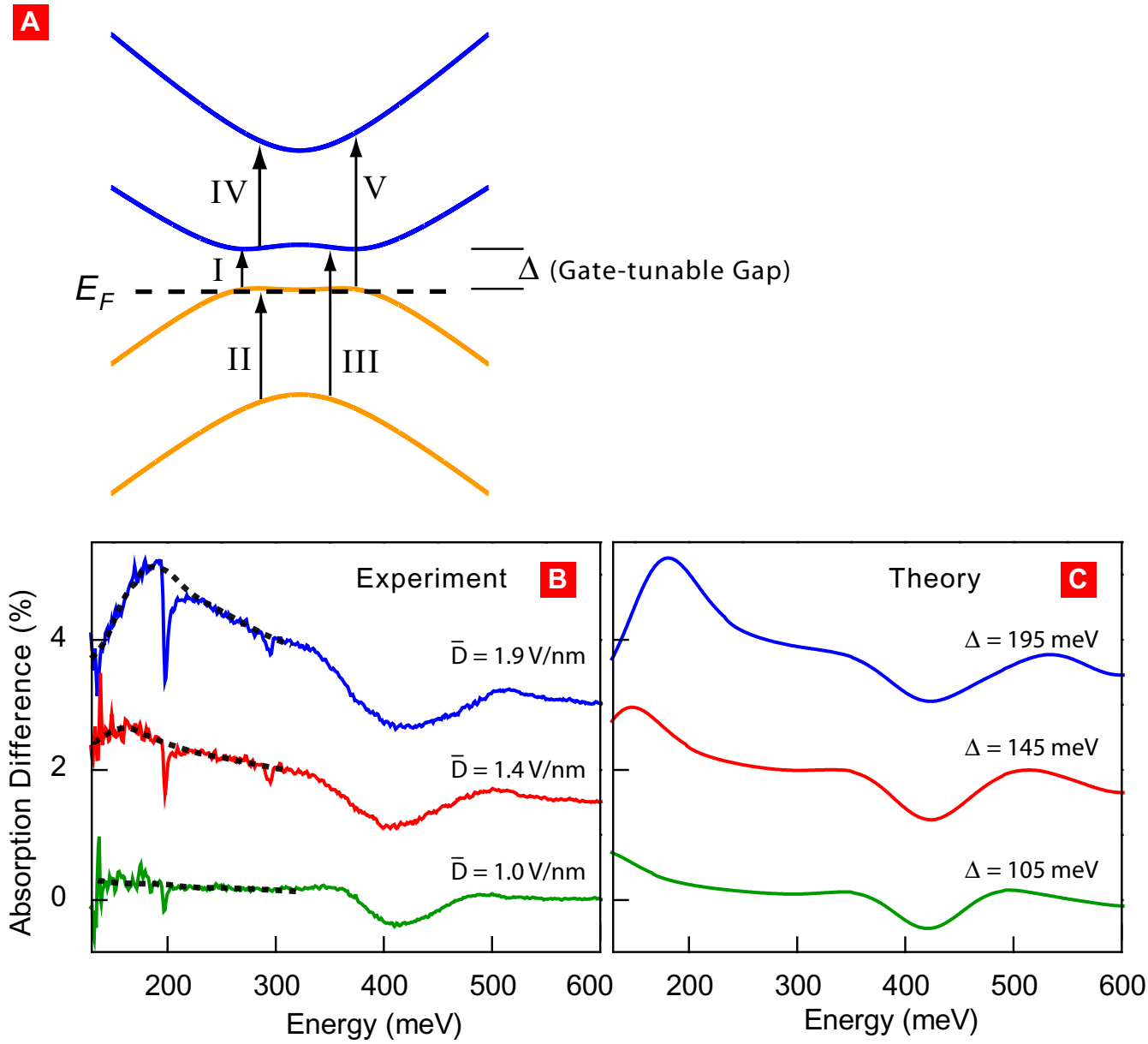
A
IV
V
I
II
III
E_F
Δ (Gate-tunable Gap)
Experiment
B
$\bar{D}$ = 1.9 V/nm
$\bar{D}$ = 1.4 V/nm
$\bar{D}$ = 1.0 V/nm
Absorption Difference (%)
4
2
0
200
300
400
500
600
Energy (meV)
Theory
C
Δ = 195 meV
Δ = 145 meV
Δ = 105 meV
200
300
400
500
600
Energy (meV)

Figure 2

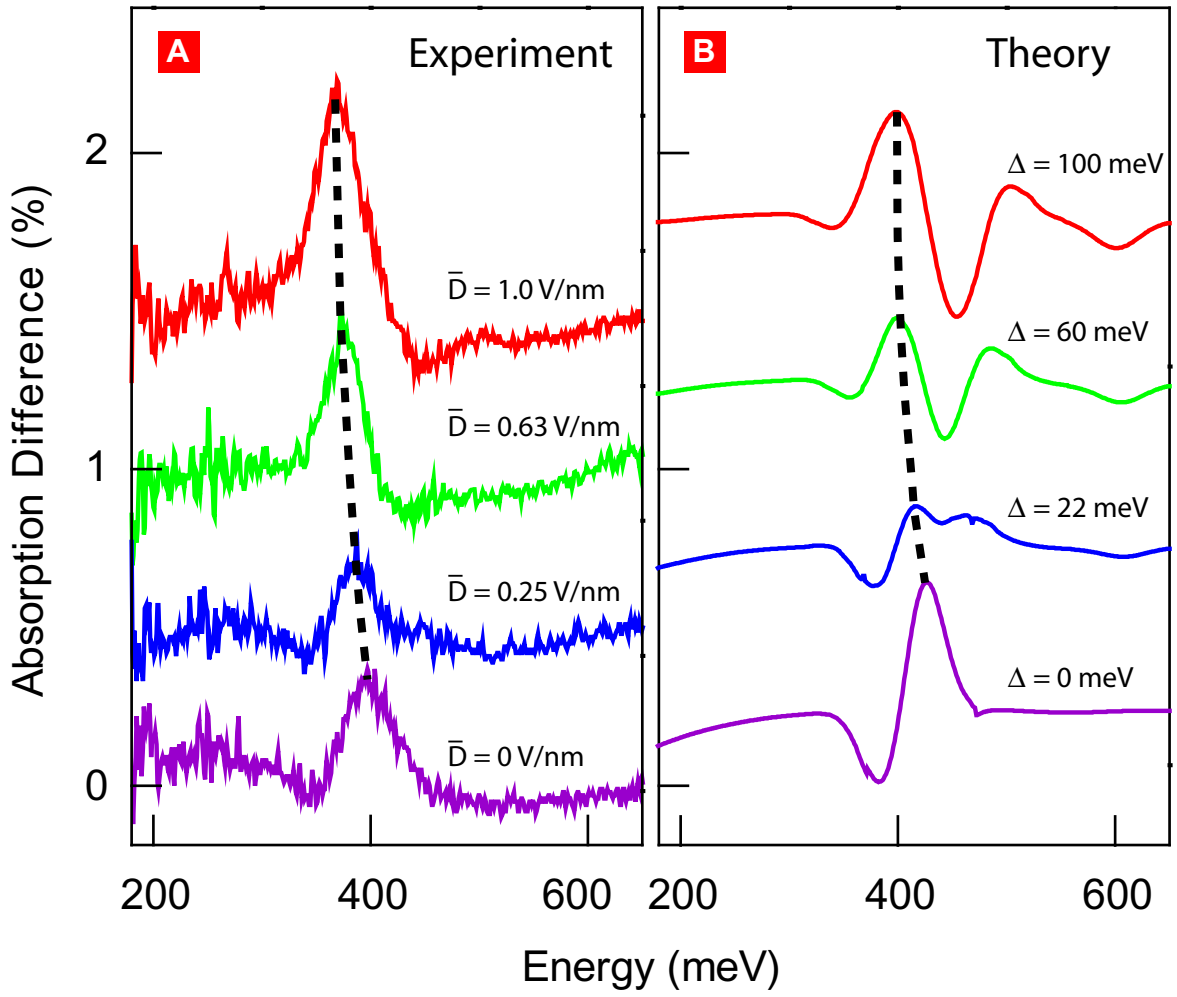
A
Experiment
B
Theory
Absorption Difference (%)
2
1
0
$\bar{D}$ = 1.0 V/nm
$\bar{D}$ = 0.63 V/nm
$\bar{D}$ = 0.25 V/nm
$\bar{D}$ = 0 V/nm
Δ = 100 meV
Δ = 60 meV
Δ = 22 meV
Δ = 0 meV
200
400
600
200
400
600
Energy (meV)

Figure 3

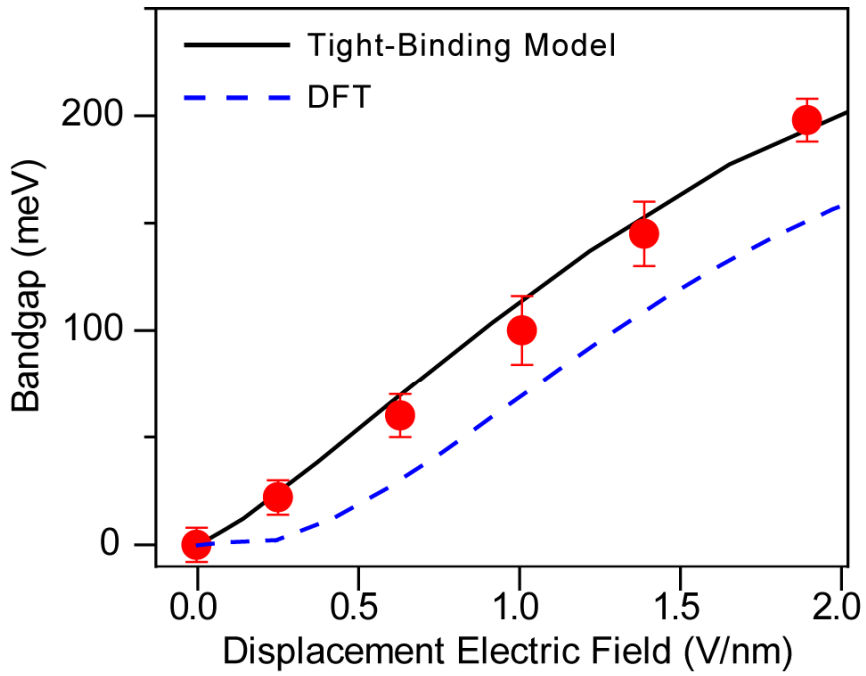
Tight-Binding Model
DFT
200
100
0
Bandgap (meV)
0.0
0.5
1.0
1.5
2.0
Displacement Electric Field (V/nm)

Figure 4

1. K. S. Novoselov *et al.*, *Nature* **438**, 197-200 (2005).
2. Y. B. Zhang, Y. W. Tan, H. L. Stormer, P. Kim, *Nature* **438**, 201-204 (2005).
3. K. S. Novoselov *et al.*, *Nature Physics* **2**, 177-180 (2006).
4. B. Huard *et al.*, *Physical Review Letters* **98**, 236803 (2007).
5. F. Miao *et al.*, *Science* **317**, 1530-1533 (2007).
6. R. R. Nair *et al.*, *Science* **320**, 1308-1308 (2008).
7. N. Stander, B. Huard, D. G. Gordon, *arXiv: 0806.2319* (2008).
8. F. Wang *et al.*, *Science* **320**, 206-209 (2008).
9. J. S. Bunch *et al.*, *Science* **315**, 490-493 (2007).
10. Z. H. Chen, Y. M. Lin, M. J. Rooks, P. Avouris, *Physica E* **40**, 228-232 (2007).
11. A. K. Geim, K. S. Novoselov, *Nature Materials* **6**, 183-191 (2007).
12. M. Y. Han, B. Ozyilmaz, Y. B. Zhang, P. Kim, *Physical Review Letters* **98**, 206805 (2007).
13. X. L. Li, X. R. Wang, L. Zhang, S. W. Lee, H. J. Dai, *Science* **319**, 1229-1232 (2008).
14. E. McCann, *cond-mat/0608221* (2006).
15. Z. Jiang *et al.*, *Physical Review Letters* **98**, 197403 (2007).
16. X. R. Wang *et al.*, *Physical Review Letters* **100**, 206803 (2008).
17. H. Min, B. Sahu, S. K. Banerjee, A. H. MacDonald, *arXiv 0612236* (2008).
18. T. Ohta, A. Bostwick, T. Seyller, K. Horn, E. Rotenberg, *Science* **313**, 951-954 (2006).
19. E. V. Castro *et al.*, *Physical Review Letters* **99**, 216802 (2007).
20. J. B. Oostinga, H. B. Heersche, X. L. Liu, A. F. Morpurgo, L. M. K. Vandersypen, *Nature Materials* **7**, 151-157 (2008).
21. Z. Q. Li *et al.*, *Nature Physics* **4**, 532-535 (2008).
22. L. M. Zhang *et al.*, *arXiv 0809.1898* (2008).
23. A. B. Kuzmenko *et al.*, *arXiv 0810.2400* (2008).
24. K. S. Novoselov *et al.*, *Proceedings of the National Academy of Sciences of the United States of America* **102**, 10451-10453 (2005).
25. A. C. Ferrari *et al.*, *Physical Review Letters* **97**, 187401 (2006).
26. D. S. L. Abergel, V. I. Fal'ko, *cond-mat/0610673* (2007).
27. D. Xiao, W. Yao, Q. Niu, *Physical Review Letters* **99**, 236809 (2007).
28. This work was supported by University of Berkeley and the Office of Basic Energy Sciences, U.S. Department of Energy under contract No. DE-AC03-76SF0098 (Materials Science Division) and contract No. DE-AC02-05CH11231 (Advanced Light Source).Y.Z. and F.W. also acknowledge support from a Miller fellowship and a Sloan fellowship, respectively. T.T.T. is partially supported by National Science Council, Taiwan.